Journal of Advanced Ceramics
2022, **11**(8): 1235–1248
https://doi.org/10.1007/s40145-022-0606-2
ISSN 2226-4108
CN 10-1154/TQ

Research Article

Ultralight and hyperelastic SiC nanofiber aerogel spring for personal thermal energy regulation

Limeng SONG[a], Bingbing FAN[a,*], Yongqiang CHEN[a,d], Qiancheng GAO[c], Zhe LI[c], Hailong WANG[a], Xinyue ZHANG[a,c], Li GUAN[c], Hongxia LI[d,*], Rui ZHANG[a,b,*]

[a]*School of Material Science and Engineering*, *Zhengzhou University*, *Zhengzhou 450001*, *China*
[b]*School of Materials Science and Engineering*, *Luoyang Institute of Science and Technology*, *Luoyang 471023*, *China*
[c]*School of Materials Science and Engineering*, *Zhengzhou University of Aeronautics*, *Zhengzhou 450015*, *China*
[d]*Sinosteel Luoyang Institute of Refractories Research Co*., *Ltd*., *Luoyang 471039*, *China*

Received: February 25, 2022; Revised: April 18, 2022; Accepted: April 27, 2022

Abstract: Multifunctionalization is the development direction of personal thermal energy regulation equipment in the future. However, it is still a huge challenge to effectively integrate multiple functionalities into one material. In this study, a simple thermochemical process was used to prepare a multifunctional SiC nanofiber aerogel spring (SiC NFAS), which exhibited ultralow density (9 mg/cm^3), ultralow thermal conductivity (0.029 W/(m·K) at 20 ℃), excellent ablation and oxidation resistance, and a stable three-dimensional (3D) structure that composed of a large number of interlacing 3C-SiC nanofibers with diameters of 300–500 nm and lengths in tens to hundreds of microns. Furthermore, the as-prepared SiC NFAS displayed excellent mechanical properties, with a permanent deformation of only 1.3% at 20 ℃ after 1000 cycles. Remarkably, the SiC NFAS exhibited robust hyperelasticity and cyclic fatigue resistance at both low (~−196 ℃) and high (~700 ℃) temperatures. Due to its exceptional thermal insulation performance, the SiC NFAS can be used for personal thermal energy regulation. The results of the study conclusively show that the SiC NFAS is a multifunctional material and has potential insulation applications in both low- and high-temperature environments.

Keywords: SiC nanofiber aerogel spring (SiC NFAS); mechanical property; thermal insulation; personal thermal energy regulation

1 Introduction

Personal thermal energy regulation technology can enable people to control their immediate thermal environment individually, leading to significantly enhanced personal thermal comfort [1–3]. Thermal comfort is the psychological state of a person who is satisfied with the surrounding environment [4]. Maintaining thermal comfort is very important to the physical and mental health of a person in extreme environmental conditions, such as in Antarctica and in steel plants. If the core body temperature is too high or too low, it may endanger human life [5]. Moreover, the

* Corresponding authors.
E-mail: B. Fan, fanbingbing@zzu.edu.cn;
H. Li, lihongx0622@126.com;
R. Zhang, zhangray@zzu.edu.cn

lack of thermal comfort may lead to a decline in labor productivity, ultimately resulting in economic recession [6]. Therefore, maintaining workers' body thermal comfort plays an important role in effectively promoting the economy [7]. Currently, indoor heating accounts for 47% of the total global energy consumption, of which 42% is dedicated to heating residential buildings [8]. A reduction in energy used for heating is critical for solving the global energy crisis [9–11]. Heating also accounts for 33.5% of the total greenhouse gas emissions, which is detrimental to the environment [8]. Significant energy savings can be achieved by using a personal thermal management system [1,12–16]. For instance, maintaining human thermal comfort within a 2 ℃ extended heating/cooling set point range can provide approximately 20% energy savings in air conditioning [7,17,18].

Personal thermal management equipment should be wearable like ordinary clothes [19–21] and be able to reduce body heat loss in cold environments and prevent external heat transfer to the skin in hot environments [22–24]. To achieve such goals, Zhao *et al*. [1] designed a thermoelectric energy conversion unit that provides cold air (cooling mode) and hot air (heating mode) to the human body through a tree-like rubber pipe network interwoven in temperature-regulating underwear. Guo *et al*. [11] developed a personal energy management device based on fluorosilane-modified textiles, which can harness mechanical energy from the human body to power wearable electronic devices and also prevent the loss of body heat while maintaining a normal body temperature. Hsu *et al*. [8] reported a metal nanowire cloth, which exhibits the wear resistance and air permeability of an ordinary cloth and has great potential in reducing indoor heating energy consumption due to personal thermal management capacity. Roh *et al*. [25] manufactured the clothes made of metal composite fabric that reflected back the body heat to the wearer as well as a large part of the outside radiation, thereby nullifying the overall impact on the body temperature. Yue *et al*. [26] prepared a multifunctional nano-silver/cellulose fiber-based thermal insulation film to realize infrared radiation insulation. Although the materials aforementioned have excellent infrared reflection properties, they have certain limitations in practical applications. Polymer-based textiles [27–29] become very hard and brittle at low temperatures, which is unconducive to the applications under extremely cold conditions. As for textiles woven from metal fibers [30–32], the high thermal conductivity of metals limits their application in high-temperature environments. As we know, SiC has superior electromagnetic characteristics [33–35], excellent optical, electronic, and thermal properties, low cost, high hardness, good stability, and environmental friendliness [36]. However, SiC nanoparticles and nanosheets are prone to agglomeration, which have certain limitations in practical applications. It is worth noting that SiC nanofibers have better electrical conductivity, a larger surface area, and better mechanical properties compared with SiC nanoparticles and nanosheets [37]. This provides an idea and inspiration for us to develop a new personal thermal energy regulation equipment to improve human thermal comfort control [7].

Therefore, in order to solve the shortcomings of the above materials in personal thermal management, we report a multifunctional SiC nanofiber aerogel spring (SiC NFAS), which can not only prevent body heat loss at low temperatures but also block external heat transfer to the body at high temperatures, thereby ensuring the safety of the wearer under extreme conditions. The aerogel spring exhibits a stable three-dimensional (3D) structure composed of numerous interwoven 3C-SiC nanofibers and is ultrathin, ultralight, and compressible. Furthermore, the aerogel spring also possesses good flame resistance, superior high/low-temperature stability, and ultralow thermal conductivity.

2 Experimental

2.1 Raw materials

The activated carbon (C, analytical grade) and calcium carbonate ($CaCO_3$, analytical grade) were purchased from Sigma-Aldrich (USA). The silicon (Si) nanopowders (200 mesh, analytical grade) and silica (SiO_2, 80 mesh, analytical grade) were purchased from Aladdin Co., Ltd. (China).

2.2 Preparation of C/$CaCO_3$ and Si/SiO_2 hybrid particles

The C/$CaCO_3$ hybrid particles were prepared by the ball mill-activated carbon and $CaCO_3$ (molar ratio = 1:1) at 300 r/min for 5 h using a UBE-F4 instrument (Hunan Ubetter Nano Technology Co., Ltd., China). The Si/SiO_2 hybrid particles were prepared under the same conditions.

2. 3 Preparation of SiC NFAS

The $C/CaCO_3$ and Si/SiO_2 hybrid particles were placed in a graphite crucible covered with a graphite lid. The inner wall of the graphite lid was used as the SiC NFAS growth substrate. The crucible was placed in a nitriding furnace (ZSL 1600X, Zhengzhou Kejing Electric Furnace Co., Ltd., China), heated to 1500 ℃ at 5 ℃/min in an argon atmosphere, and held at 1500 ℃ for 5 h. During this step, the generated SiO and CO gases formed SiC fibers on the surface of the graphite lid. Finally, the graphite lid was placed in a muffle furnace and heated at 700 ℃ in an air atmosphere for 5 h. The SiC NFAS was exfoliated from the surface of the graphite lid after cooling to room temperature. The fabrication process of the SiC NFAS is shown in Fig. 1.

2. 4 Characterization

The microscopic structures of the SiC NFAS were characterized using the scanning electron microscope (SEM; JSM-7001F, Japan Electronics Corporation, Japan) at 15 kV and the field-emission transmission electron microscope (TEM; JEM-2100F, Japan Electronics Corporation, Japan) at 200 kV. The crystal structures of the SiC NFAS were characterized via the X-ray diffractometer (Smartlab, Rigaku Corporation, Japan) with Cu Kα radiation (λ = 0.154 nm) at 40 kV. The surface groups and elemental states of the samples were qualitatively detected using the Fourier-transform infrared (FTIR) spectrometer (Nicolet iS10, Thermo Fisher Scientific, USA) in the wavenumber range of 4000–400 cm^{-1} and the X-ray photoelectron spectrometer (EscaLab Xi+, Thermo Fisher Scientific, USA), respectively. The samples were heated to 1350 ℃ (heating rate: 20 ℃/min) in the air in the thermogravimetric analyzer (STA 409 PC/4/H, NETZSCH-Gerätebau GmbH, Germany). The Raman spectra were obtained using a confocal Raman microscope (LabRAM HR Evolution, HORIBA Jobin Yvon S.A.S., France). An electronic universal testing machine (JHYC, Nanjing Juhang Technology Co., Ltd., China) was used to measure the compressive strength of the as-prepared samples. The thermal conductivities were measured using the transient hot-wire instrument (HCDR-S, Nanjing Huicheng Instruments Co., Ltd., China) in a testing range of 0.001–10.0 W/(m·K). The heat transfer process in the samples was visualized using an infrared imaging system (FLIR E750, FLIR Systems, USA).

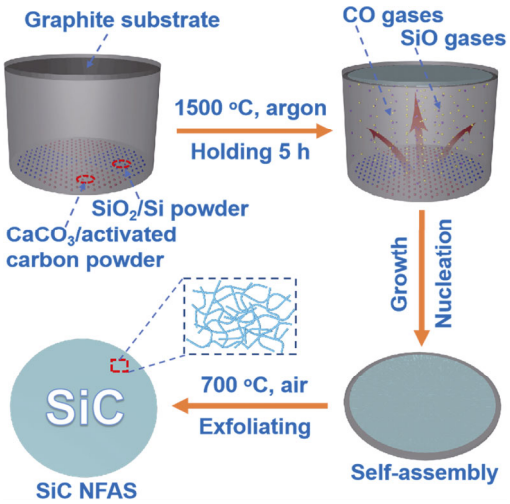

Fig. 1 Schematic illustration of the preparation of the SiC NFAS.

3 Results and discussion

3. 1 Preparation and characterization of SiC NFAS

SiC fibers are prepared by the chemical vapor deposition (CVD) and then interwoven and stacked to form the SiC NFAS. As shown in Fig. 2(a), the SiC NFAS was prepared in a vacuum nitriding furnace at 1500 ℃ under a constant argon gas pressure of 0.25 MPa. During this process, a comproportionation reaction occurred between Si and SiO_2 to generate SiO gas (Reaction (1)); meanwhile, CO_2 gas was generated from the thermal decomposition of $CaCO_3$ (Reaction (2)). The activated carbon reacted with the generated CO_2 to form CO gas (Reaction (3)). To maintain a pressure balance inside and outside of the crucible, the as-generated SiO and CO gases flowed out of the crucible along the paths, as shown by the red arrows in Fig. 2(a), and provided Si and C sources for the nucleation and growth of SiC nanofibers (Reaction (5)) on the inner surface of the graphite lid. The graphite carbon of the lid acted as a growth site for SiC formation (Reaction (4)). It is noteworthy that the nucleation sites and growth directions of SiC fibers are random, resulting in that SiC fibers are randomly grown on the surface of the graphite lid. Finally, the SiC nanofibers were heated at 700 ℃ for 5 h in an air atmosphere to separate them from the graphite lid. The as-prepared fibers had a 3C-SiC cubic crystal structure [38]. The reactions can be described as

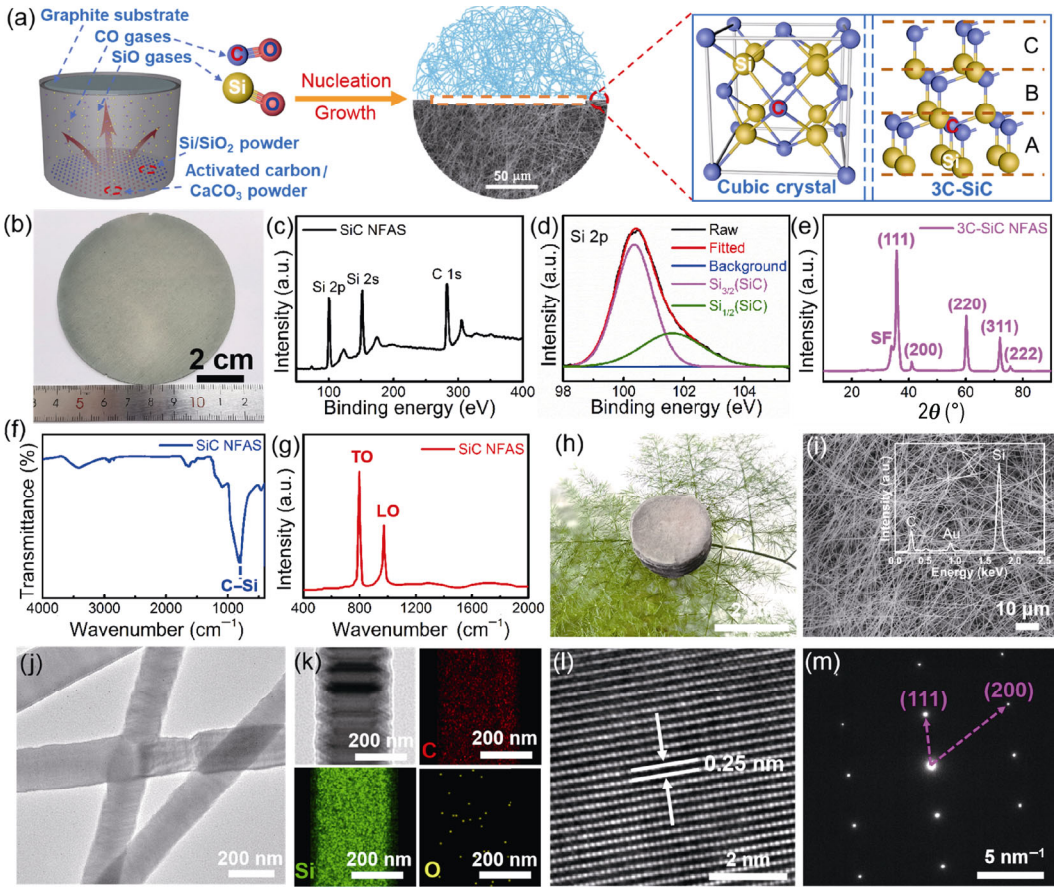

Fig. 2 Macro and micro characters, crystal structures, and chemical compositions of the SiC NFAS. (a) Schematic illustration of SiC NFAS fabrication and corresponding atomic structure model. (b) Digital photograph of a SiC NFA disc. (c) X-ray photoelectron spectroscopy (XPS) spectrum and (d) deconvoluted Si 2p peaks of the SiC NFAS. (e) X-ray diffraction (XRD) pattern, (f) FTIR spectrum, and (g) Raman spectrum of the SiC NFAS. (h) Sample of SiC NFAS placed on an *Asparagus setaceus* (Kunth) Jessop. (i) SEM image and energy-dispersive spectroscopy (EDS) (the inset) spectrum of the SiC NFAS. (j) TEM image and (k) corresponding C, Si, and O elemental mappings of the SiC fibers. (l) High-resolution TEM (HRTEM) image and (m) selected area electron diffraction (SAED) pattern of a SiC fiber. Note: A, B, and C in (a) are the three arrangements of Si and C atoms.

$$Si(s) + SiO_2(s) \rightarrow 2SiO(g) \quad (1)$$

$$CaCO_3(s) \xrightarrow{\Delta} CO_2(g) + CaO(s) \quad (2)$$

$$CO_2(g) + C(s) \rightarrow 2CO(g) \quad (3)$$

$$SiO(g) + 2C(s) \rightarrow SiC(s) + CO(g) \quad (4)$$

$$SiO(g) + 3CO(g) \rightarrow SiC(s) + 2CO_2(g) \quad (5)$$

A circular SiC NFA disc with an area of approximately 45 cm^2 is shown in Fig. 2(b). The XPS spectrum in Fig. 2(c) displays a C 1s peak at 283.1 eV and two peaks of Si at 100.1 and 152.1 eV corresponding to Si 2p and Si 2s, respectively, indicating the successful synthesis of SiC NFAS. When deconvoluted, Si 2p (Fig. 2(d)) reveals two peaks, Si $2p_{3/2}$ at 100.5 eV and Si $2p_{1/2}$ at 101.6 eV, of SiC [39]. The crystallographic structure of the SiC nanofibers was investigated using the XRD. The pattern (Fig. 2(e)) shows the peaks assigned to the (111), (200), (220), (311), and (222) planes of 3C-SiC (JCPDS Card No. 29-1129) [40], and a weak peak located at the shoulder of the (111) plane, which was attributed to the stacking faults (SF) of the rotational twin structure along the (111) plane direction. The atomic model of the defect is schematically shown in Fig. S1 in the Electronic Supplementary Material (ESM). The FTIR spectrum (Fig. 2(f)) distinctly shows the Si–C peak at approximately 815 cm^{-1}. The Raman spectrum (Fig. 2(g)) shows two peaks at 798.7 and 973.2 cm^{-1}, corresponding to the absorption bands from transversal optic (TO) and longitudinal optic (LO) mode Si–C vibrations at the Γ point of cubic SiC [41], respectively, which suggested a single-crystalline 3C-SiC structure of the nanofibers. As shown in Fig. 2(h), the self-adherent bulk SiC aerogel was so light

that it could stay on an *Asparagus setaceus* (Kunth) Jessop, reflecting its ultralow density (~9 mg/cm^3) and high porosity (~99.5%), as presented in Table S1 in the ESM. The SEM analysis (Fig. 2(i)) reveals a highly porous structure of the SiC NFAS. The nanofibers had diameters of 300–500 nm and lengths of tens to hundreds of microns. The EDS spectrum shows that the composition was mainly C and Si (the inset of Fig. 2(i)). The TEM analysis (Fig. 2(j)) provides a clearer image of the microstructures of the nanofibers. Furthermore, the sectional TEM image of a SiC nanofiber (Fig. 2(k)) and its corresponding elemental mappings confirmed that the SiC nanofiber is mainly composed of C (red dots) and Si (green dots) elements along with a small amount of O (yellow dots) on the surface, which could be attributed to a small number of SiO and SiO_2 particles. The HRTEM image (Fig. 2(l)) reveals the interplanar spacing in SiC nanofibers to be 0.25 nm, corresponding to the (111) plane of 3C-SiC [42]. The corresponding SAED pattern (Fig. 2(m)) indicates that the SiC NFAS was composed of single-crystalline SiC nanofibers [43].

3.2 Compression tests of SiC NFAS at different temperatures

Mechanical robustness is crucial for personal thermal energy regulation of the SiC NFAS. After different temperature treatments, the SiC NFAS can still withstand large compressive deformation with only small permanent deformation. As shown in Fig. 3(a), the SiC NFAS could be easily compressed into a tablet and then recovered after releasing the compression. Figure 3(b) shows the stress–strain curves at 10%, 20%, 40%, and 60% strains, and the SiC NFAS recovered its original configuration even after 60% strain. Similar to the deformation behavior of some other nanofiber aerogels, the loading process of the NFAS had two different stages [44]: a linear elastic regime at strain < 40% with an elastic modulus of ~28.92 kPa and a nonlinear regime with a steep rise in stress. This resilient compressibility was further highlighted by a durable cyclic performance at 60% strain with a high strain rate of 80 mm/min (Fig. 3(c)). The SiC NFAS with a combination of the ceramic nature and nanofiber architecture is promising for achieving

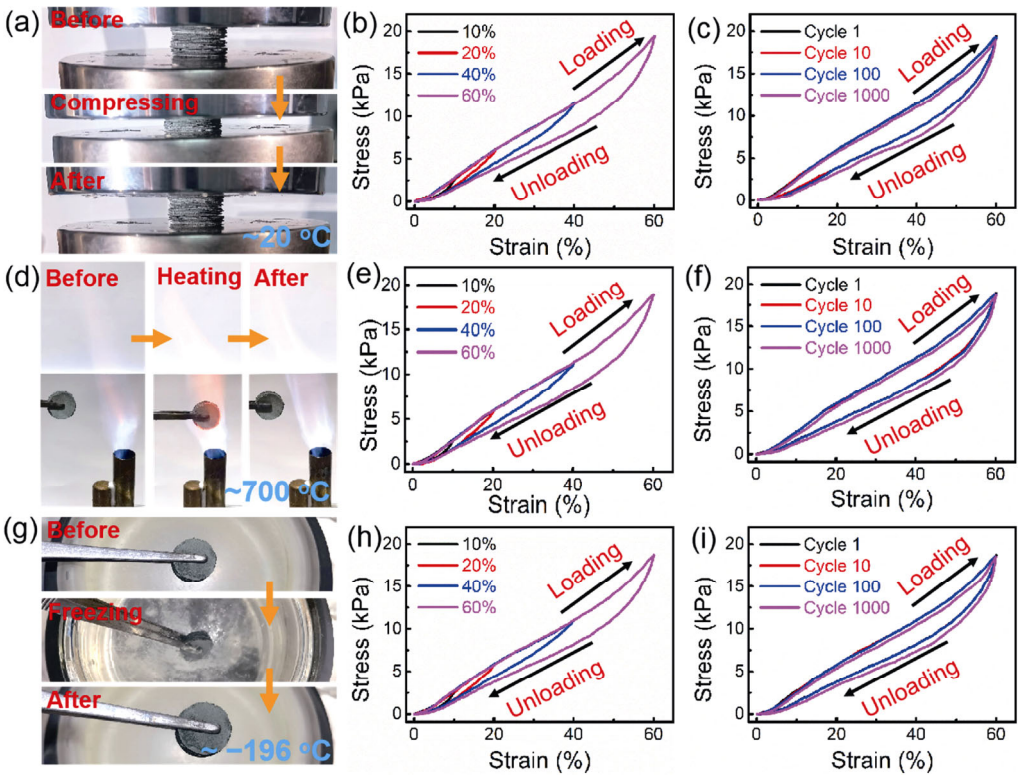

Fig. 3 Mechanical properties of SiC NFAS under various temperatures. The high compressibility of the SiC NFAS at (a) room temperature (~20 ℃), (d) high temperature (~700 ℃), and (g) low temperature (~ −196 ℃). Compressive stress–strain curves of the SiC NFAS at (b) room temperature, (e) high temperature, and (h) low temperature. Cyclic compressive stress–strain curves of the SiC NFAS at (c) room temperature, (f) high temperature, and (i) low temperature.

temperature-invariant hyperelasticity [45]. Moreover, cross section SEM images of before and after the 1000-circle compression are exhibited in Figs. S2(a) and S2(b) in the ESM, respectively. It can be seen that the cross section microstructure is nearly the same before and after the 1000-circle compression experiment. The formed SiC fibers are randomly arranged and assembled into 3D SiC NFAS, due to the random growth mechanism. The SiC nanofibers are isotropy in the SiC NFAS, which causes its excellent mechanical properties. The high-temperature hyperelasticity of SiC NFAS was demonstrated by the compression testing after the heat treatment with an alcohol torch (~700 ℃, Fig. 3(d)). As expected, the stress–strain curve after high-temperature treatment (Fig. 3(e)) showed a deformation trend similar to that of the original SiC NFAS. The heat-treated aerogel also endured 1000 fatigue cycles at 60% strain with a strain rate of 80 mm/min (Fig. 3(f)). This high loading–unloading speed confirmed the rapid elastic recovery property of the SiC NFAS. After 1000 cycles, the NFAS retained most of its macroscopic shape with only a slight permanent deformation of 1.3%. In addition, the SiC NFAS also demonstrated robust hyperelasticity at low temperatures (~ −196 ℃) under liquid nitrogen conditions, as shown in Fig. 3(g). The stress–strain curves of SiC NFAS (Fig. 3(h)) at 10%, 20%, 40%, and 60% strain were similar to those at room temperature, indicating the excellent hyperelasticity of SiC NFAS even after direct immersion in liquid nitrogen. Despite low-temperature treatment, the aerogel also exhibited good cyclic fatigue resistance (strain rate: 80 mm/min), as depicted in Fig. 3(i).

The maximum stress and Young's modulus during cyclic compression [46] of SiC NFAS treated at different temperatures are shown in Fig. S3 and Table S2 in the ESM. For the first cycle, the maximum stress and Young's modulus at room temperature were 19.45 and 28.75 kPa, respectively. After 1000 cycles, the maximum stress and Young's modulus were 18.72 and 27.61 kPa, respectively, which confirmed a nearly constant compressive strength. For the heat-treated SiC NFAS, the maximum stress and Young's modulus were 18.91 and 28.16 kPa in the first cycle, respectively. Yet, after 1000 cycles, the maximum stress and Young's modulus were only 18.31 and 27.30 kPa, respectively. Notably, the maximum stress and Young's modulus of the SiC NFAS immersed in liquid nitrogen were 18.17 and 26.06 kPa after 1000 cycles, respectively, similar to that in the first cycle. These results highlight the excellent mechanical performance of SiC NFAS.

3.3 Flexibility, elasticity, and structural robustness of SiC NFAS

The flexibility, elasticity, and structural robustness are inherent properties of SiC fibers. And the SiC NFAS with 3D structure also possesses these properties, which are very important for practical applications of ceramic aerogels. To further verify the excellent mechanical property of the obtained SiC NFAS, the microstructure evolution during the compression and recovery process is observed in the *in-situ* SEM images. A series of sequential SEM images during the SiC NFAS compression are shown in Figs. 4(a)–4(d). When the compression deformation is ~10%, there are no obvious signs of structural changes in Fig. 4(a). As the compressive strain increases to ~40%, the SiC nanofibers move along the compression direction and deform significantly under stress (Fig. 4(b)). Under ~60% compressive strain, the SiC fibers move to their lowest position (the position of red circular dashed line), and their bending curvature becomes larger (marked by red dashed line), as shown in Fig. 4(c). Although the compression strains are high, the SiC NFAS keeps the original 3D structure, and the main apparent features of aerogel remain unchanged under increasingly high stress. The large bending deformation of the SiC NFAS is considered a synergistic effect of the flexibility of the SiC fibers and the highly porous structure of the aerogel. As exhibited in Fig. 4(d), when the stress is unloaded, the compressed aerogel returns to its original shape without any damage or deformation, and SiC fibers in the SiC NFAS recover their original shape and position. In brief, the excellent elasticity and compressibility of SiC NFAS can be attributed to the inherent flexibility of fibers, the highly porous structure of aerogels, and the robustness of SiC [47]; therefore, the SiC NFAS shows a good damage-tolerance even under maximum compression. As presented in Figs. 4(e)–4(g) and Figs. S4(a) and S4(b) in the ESM, the as-prepared SiC NFAS also exhibits good resistance to bending, twisting, and curling in terms of macromechanics, confirming their superior flexibility, elasticity, and structural robustness. Furthermore, to clarify the mechanism of the elasticity, the schematic illustration of SiC NFAS demonstrates the microstructure evolution during the compression and releasing process, as shown in Figs. 4(h)–4(j). It

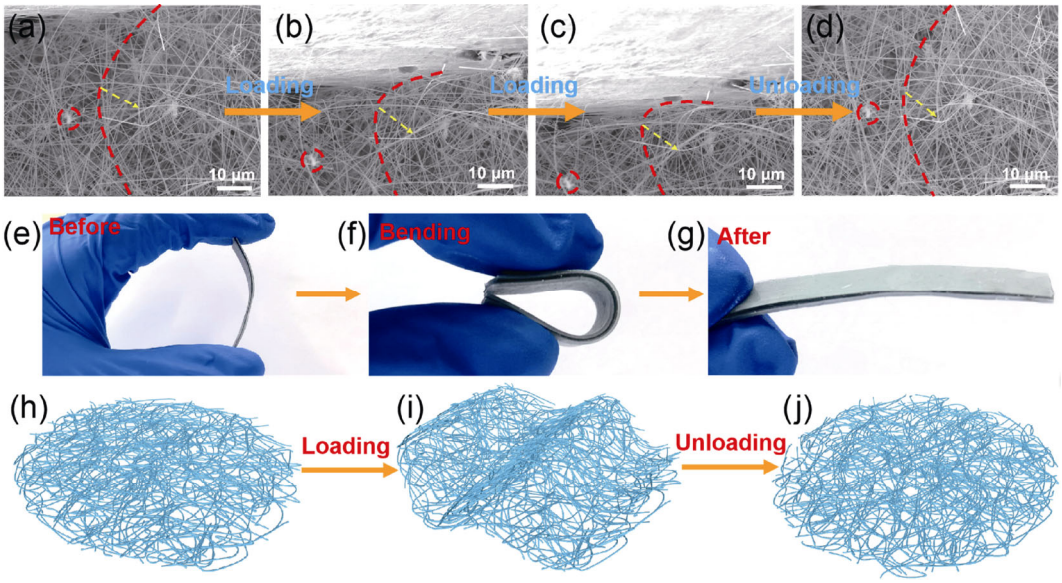

Fig. 4 Microstructure evolution and demonstration of the flexibility of SiC NFAS during the compression and recovery process. SEM images of compression deformation: (a) ~10%, (b) ~40%, and (c) ~60% deformation. (d) SEM image of SiC NFAS after full recovery. The marked red circles and curves indicate the change in displacement during the compression and recovery processes, respectively. (e–g) Bending process of SiC NFAS. (h–j) Demonstration of the flexibility of SiC NFAS.

can be seen intuitively that the SiC NFAS possesses good resistance to bending, further reflecting their mechanical flexibility and structural robustness.

3. 4 High-temperature chemical and thermal stability of SiC NFAS

The as-prepared SiC NFAS has superior chemical and thermal stability at high temperatures, which is crucial for the application at high temperatures. A sample of SiC NFAS exhibited excellent fire retardancy and thermal stability when exposed to the flame of an alcohol burner for more than 10 min, as demonstrated in Fig. 5(a). The excellent thermal and chemical stability of SiC NFAS in the air was further exemplified by its thermogravimetric analytical (TGA) thermogram (Fig. 5(b)), where the weight of the sample remained almost constant till 925 ℃. However, the weight gain was observed after 925 ℃ owing to the oxidation of SiC (Reaction (6)) [48]. After 1275 ℃, the weight remained nearly constant as the oxidation of the SiC nanofibers was complete. The corresponding results are presented in Table S1 in the ESM.

$$SiC(s) + 2O_2 \rightarrow SiO_2(s) + CO_2(g) \quad (6)$$

The SiC NFAS also exhibited excellent thermal insulation properties. A SiC NFAS sample with a thickness of ~10 mm could protect a fresh flower from fading or carbonization when heated for 10 min, as shown in Fig. 5(c). In comparison, the flower was fully carbonized within 20 s without the protection of the SiC NFAS (Fig. S5 in the ESM). The thermal conductivities of the SiC NFAS in an argon atmosphere at various temperatures are presented in Fig. 5(d) and Table S3 in the ESM. Notably, the room-temperature thermal conductivity was only 0.029 W/(m·K), suggesting that the material is an excellent thermal insulator. The thermal conductivity increased with the increasing temperature with thermal conductivities at 200 and 600 ℃ being 0.045 and 0.112 W/(m·K), respectively. To further explore the thermal insulation performance of SiC NFAS, a sample was placed on a heating stage. Figure 5(e) shows the real-time temperatures measured from the side of the SiC NFAS after 10 min. The temperatures of the top (Sp1), middle (Sp2), and bottom (Sp3) were 130.4, 211.4, and 324.4 ℃, respectively. The temperature of the top was lower than those of the bottom and middle and reached a relatively stable value of ~130 ℃ after 5 min under the same heating conditions. The corresponding real-time temperatures recorded as a function of time are shown in Fig. 5(f). Figure 5(g) shows the top-side real-time temperature of the SiC NFAS sample. The corresponding temperatures of the edge (Sp1), aerogel (Sp2), and heating platform (Sp3) were 175.9, 129.1, and 405.1 ℃ after 10 min, respectively. The temperature of the aerogel plateaued at ~130 ℃ after 5 min, as evident from the

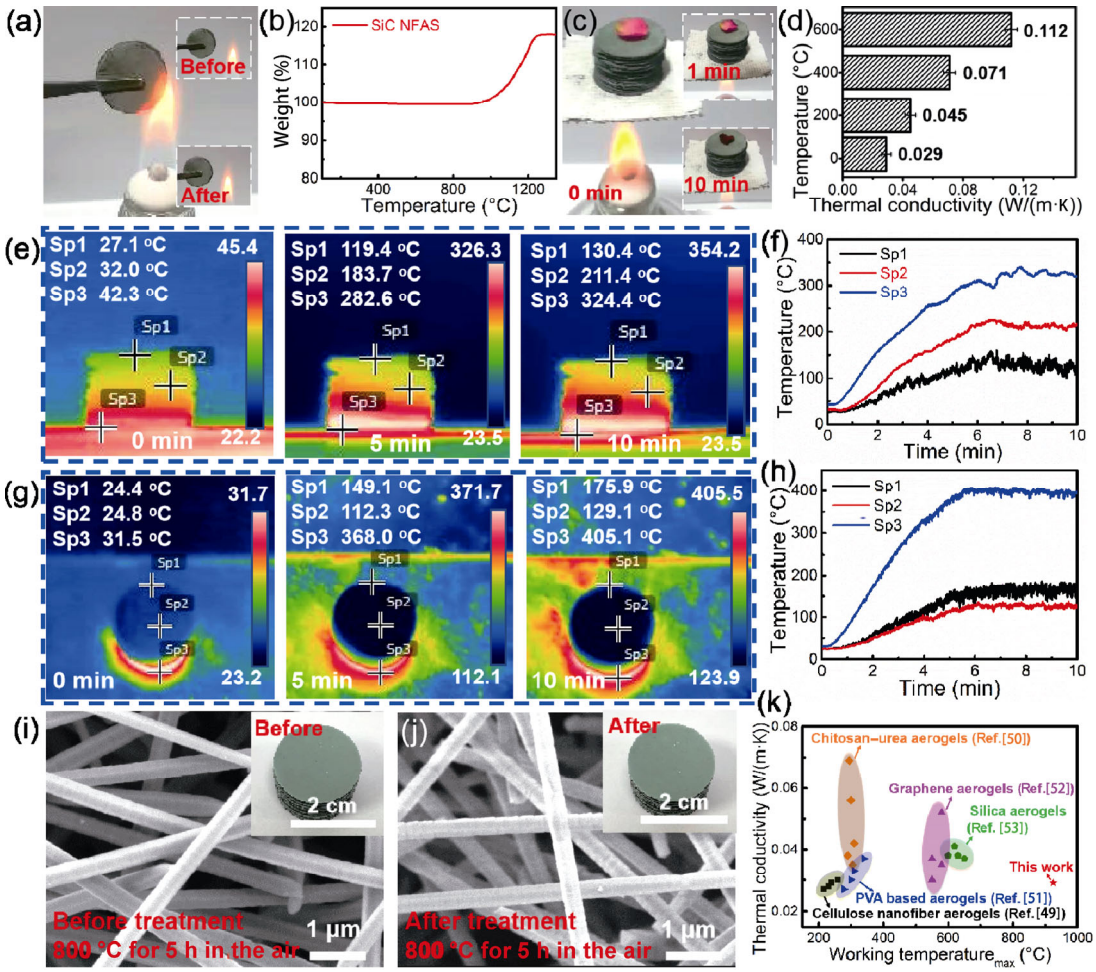

Fig. 5 Thermal and chemical stability tests of SiC NFAS. (a) Digital photographs of the SiC NFAS, as it was subjected to a burner flame. (b) TGA curve of the SiC NFAS. (c) Digital photographs of a flower placed on the SiC NFAS, which was heated over a burner. (d) Thermal conductivities of the SiC NFAS at various temperatures in an argon atmosphere. Thermal images of the SiC NFAS during heating on a heated platform from (e) side and (g) top with (f, h) corresponding temperature vs. time curves, respectively. SEM images of a SiC NFAS sample (i) before and (j) after heating at 800 ℃ in the air for 5 h with the insets showing digital photographs of the corresponding sample. (k) Room-temperature thermal conductivities in the air vs. maximum working temperature for various aerogel materials.

corresponding real-time temperature vs. time graph (Fig. 5(h)). These results further confirmed the outstanding thermal insulation property of SiC NFAS. Finally, the SiC NFAS was heated in a furnace in an air atmosphere at 800 ℃ for 5 h. It can be seen that the appearance of SiC NFAS remained well preserved even after heating (the insets of Figs. 5(i) and 5(j)). Microscopically, the structure remained highly porous (Fig. 5(j)) similar to the original one (Fig. 5(i)), confirming the excellent thermal stability. The prepared SiC NFAS exhibited much superior performance in terms of thermal conductivity and excellent thermal and chemical stability compared to those of recently reported aerogels based on cellulose nanofiber [49], chitosan–urea [50], polyvinyl alcohol (PVA) composite [51], graphene [52], and silica [53] (Fig. 5(k)). These integrated properties make SiC NFAS one of the most excellent thermal insulation materials for demanding applications, such as thermal insulation of buildings and thermal protection of aerospace vehicles.

3. 5 Thermal insulation properties of SiC NFAS at normal temperatures

The SiC NFAS possesses excellent thermal insulation property, which is one of the important factors for a superior personal thermal energy regulation equipment. The passive radiative heating property of the SiC NFAS can be evaluated by the radiative heat loss from

the SiC NFAS to the surrounding environment [54]. Figures 6(a) and 6(b) show the measured reflectivity and transmissivity curves of SiC NFAS samples with various thicknesses, respectively. Figure S6 in the ESM is presented based on the thermal radiation relation: $\varepsilon = 1 - \rho - \tau$, where ε, ρ, and τ are the absorptivity, reflectivity, and transmissivity, respectively. Macro-level reflection is primarily related to the length of the SiC fibers, and the maximum reflectivity occurs when the length of the SiC fibers is similar to the radiation wavelength. The SiC NFAS is composed of SiC fibers with the lengths ranging from a few microns to hundreds of microns. Therefore, the SiC NFAS can effectively reflect the mid-infrared (2.5–25 μm) radiation, as shown in Fig. 6(a). In addition, SiC is a wide-band-gap (E_g = 2.38–3.26 eV) semiconductor material [55] with excellent photoelectric properties. As pure SiC has a high resistivity, its carrier concentration is determined by the defects. The SiC grain boundary barrier induces carrier scattering because of its high specific surface area. The intraband mid-infrared scattering by the SiC fibers is dominant, and the electron scattering mechanism between bands and intraband elastic scattering leads to strong linear scattering (Rayleigh scattering) [56]. Nonlinear scattering (Raman scattering) [57] also plays a crucial role in the mid-infrared scattering by SiC NFAS, which is strongly dependent on the carrier density of the Fermi energy [58]. Hence, the micro-level reflection was attributed to the crystal structure of SiC. Specifically, the average mid-infrared spectral reflectivity at 7–14 μm (human body infrared radiation wavelength) of ~10-mm-thick sample was calculated to be 95.7%, which is higher than those of ~1-mm-thick (94.6%), ~3-mm-thick (94.9%), and ~5-mm-thick samples (95.2%). Conversely, the average mid-infrared spectral transmissivity at 7–14 μm of the ~10-mm-sample was calculated to be 0.98%, which is much lower than those of ~1-mm-thick (1.23%), ~3-mm-thick (1.19%), and ~5-mm-thick (1.14%) samples. A digital spiral micrometer (IP65, Guilin Guanglu Digital Measurement

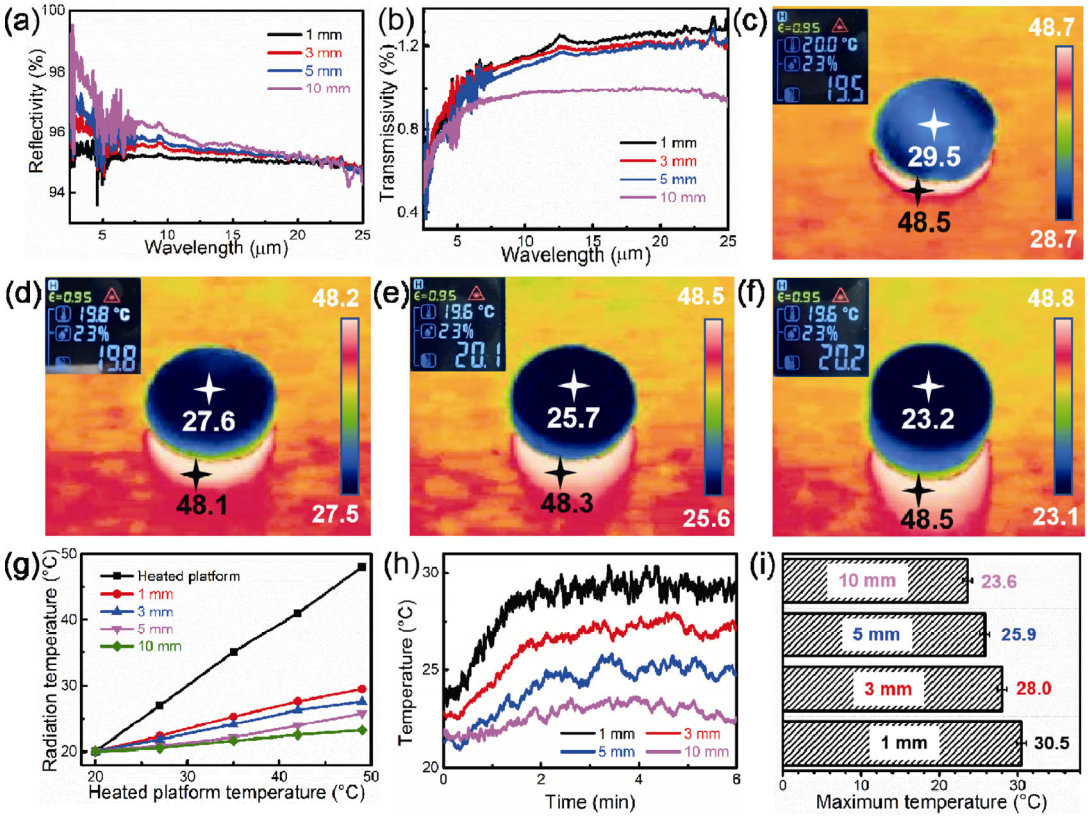

Fig. 6 Thermal insulation properties of SiC NFAS with various thicknesses. (a) Infrared reflectivity and (b) infrared transmissivity of the SiC NFAS at ~1, ~3, ~5, and ~10 mm thicknesses. Thermal images of (c) ~1-, (d) ~3-, (e) ~5-, and (f) ~10-mm-thick SiC NFAS when placed on a heated platform with a temperature of ~48.5 ℃. (g) Radiation temperatures of SiC NFAS with various thicknesses placed on a heated platform with different temperatures. (h) Real-time temperatures of ~1-, ~3-, ~5-, and ~10-mm-thick SiC NFAS. (i) Maximum temperatures of the SiC NFAS with various thicknesses when placed on a heated platform.

and Control Co., Ltd., China) was used to measure the thickness of the SiC NFAS samples, as shown in Figs. S7(a)–S7(d) in the ESM. As shown in Figs. 6(c)–6(f), when the maximum temperature reached 48.5 ℃, the radiation temperatures of the ~1-, ~3-, ~5-, and ~10-mm-thick samples placed on the heated platform were 29.5, 27.6, 25.7, and 23.2 ℃, respectively. The corresponding stable radiation temperatures are shown in Fig. 6(g). At the same heated platform temperature, the radiation temperature gradually decreased with the increasing thickness of the SiC NFAS sample. The real-time temperatures of the samples are shown in Fig. 6(h), from which it is evident that the temperature of the ~10-mm-thick sample increased much slower than those of the others. The corresponding maximum attained temperatures are presented in Fig. 6(i). As expected, all the samples showed a significant reduction in the radiation temperature compared to the heated platform. This remarkable phenomenon proved the excellent infrared radiation insulation performance of the SiC NFAS near the human body temperature and provided us with ideas for the practical application of the SiC NFAS, as described in Section 3.6.

3. 6 SiC NFAS as personal thermal energy regulation equipment verification

To further study the insulation effect of SiC NFAS on the human body, an experiment was conducted in an outdoor environment. The weather condition was sunny at 12:00, and the corresponding real-time temperature (11.7 ℃) was recorded using an infrared thermometer (GIS 500, Bosch, Germany), as shown in Fig. 7(a). A ~1-mm-thick SiC NFAS sample (Fig. S8(a) in the ESM) was placed on a healthy human head, and the corresponding radiation temperature was found to be nearly close to the ambient temperature (12.7 ℃) and much lower than the actual temperature of the hand (35.0 ℃), as shown in Fig. 7(b). This experiment was repeated at midnight (00:00), and the corresponding real-time temperature was 5.7 ℃ (Fig. 7(c)). It can be clearly seen in Fig. 7(d) that the radiation temperature of the hand covered with the SiC NFAS (5.8 ℃) was far lower than that of the hand (25.6 ℃). The SiC NFAS sample (thickness: 1.006 mm, Fig. S9(a) in the ESM) was further used to cover different parts of the human body (head, arm, anterior thoracic, and ankle) in an outdoor environment (Figs. S8(a)–S8(i) in the ESM). The results showed that the surface temperature of the human body covered by the SiC NFAS was significantly lower than the normal temperature of the human body, demonstrating a very outstanding heat insulation performance of the SiC NFAS on a real human body. Figure 7(e) shows a thermal image and digital photograph (the inset) of a hand covered with a piece of cotton (thickness: 1.079 mm, Fig. S9(b) in the ESM) at midday (12:00). Although the radiation temperature on the surface of the cotton (25.6 ℃) was lower than that of the hand (35.5 ℃), it was still much higher than that of the hand covered with the SiC NFAS (12.7 ℃) under the same conditions. Similarly, the radiation temperature on the surface of the cotton (12.3 ℃) was significantly higher than that of the hand covered with the SiC NFAS at night (00:00). A piece of leather (thickness: 1.181 mm, Fig. S9(c) in the ESM) was also used to compare the thermal insulation effect on the hand at midday (Fig. 7(g)). As expected, the radiation temperature of the hand covered with the leather (26.8 ℃) was lower than that of the hand (35.1 ℃); however, it was far higher than that of the SiC NFAS (12.7 ℃). At night, the radiation temperature on the surface of the leather (13.6 ℃) was also higher than that of the SiC NFAS. Figures 7(i) and 7(j) display thermal images and digital photos (the insets) of a piece of wool (thickness: 1.182 mm, Fig. S9(d) in the ESM) on the hand at 12:00 and 00:00, respectively. Undoubtedly, the radiation temperatures on the surface of the wool were higher than those of the SiC NFAS under the same conditions. These results suggest a superior thermal insulation effect of the SiC NFAS on the human body compared to other common insulation materials. Therefore, the SiC NFAS can be used as a thermal insulation material for personal thermal energy regulation, particularly in cold environments.

The SiC NFAS can also be cut into various shapes owing to its superior flexibility. The letters “SiC” cut from the SiC NFAS are clearly visible in the thermal image against a heated platform (~101 ℃), suggesting that SiC NFAS has great potential in blocking infrared signal transmission. To ensure the rigor of the experiment, the thermal images of the body of a person were obtained. Figures 7(l) and S8(e) in the ESM show the thermal images of the person at 12:00 and 00:00, respectively. Figure 7(m) shows the temperature variation in a 24-h period on November 9, 2021 (obtained from https://weather.cma.cn/web/weather/57083.html). The possible application of SiC NFAS in extremely cold weather is illustrated in Fig. 7(n), in which a cute penguin wearing SiC NFAS clothes stands

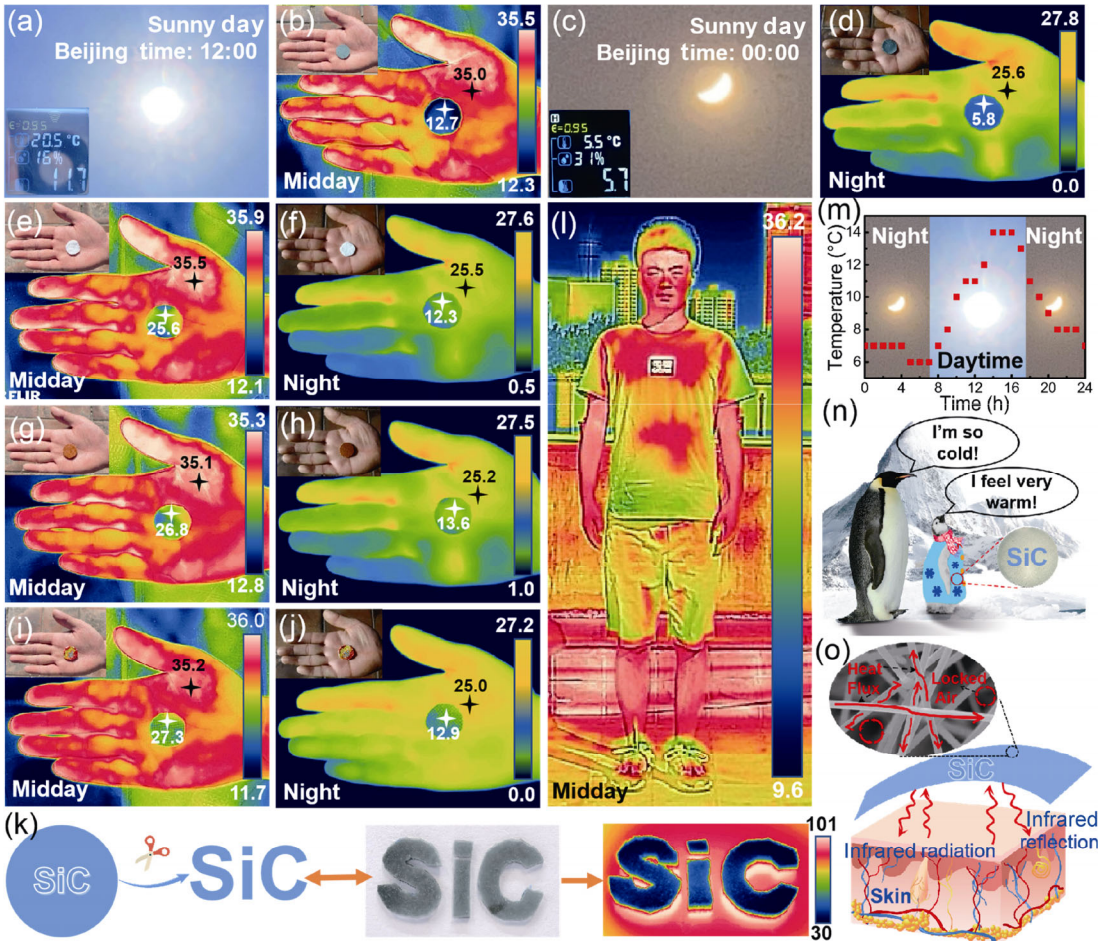

Fig. 7 SiC NFAS for personal thermal energy regulation. Digital photographs of real-time weather conditions at (a) 12:00 and (c) 00:00 on a sunny day with the insets showing the real-time temperatures. Thermal images of a healthy human hand covered with a piece of (b, d) SiC NFAS (1.006 mm), (e, f) cotton (1.079 mm), (g, h) leather (1.181 mm), and (i, j) wool (1.182 mm). (k) Images of "SiC" letters directly cut from a piece of SiC NFAS. (l) Thermal image of a healthy person. (m) Real-time temperatures over a period of 24 h (November 9, 2021). (n) Application demonstration of SiC NFAS in extremely cold weather. (o) Schematic of infrared radiation and reflection between human skin and the SiC NFAS, with the inset exhibiting the SEM image of the SiC NFAS.

on the glacier in Antarctica, and sincerely sighs that it is very warm. Therefore, this is very useful when people or other animals need to be kept warm in extremely cold environments. The human body continuously produces heat through metabolism and radiates heat to the environment to maintain the body temperature. Heat dissipation usually occurs through four different pathways: radiation, conduction, convection, and evaporation [59]. Generally, when people are in a cold environment and do not exercise vigorously, the loss of body heat is mainly caused by the loss of radiant heat in the mid-infrared wavelength range [7,28,60]. The SiC NFAS can effectively prevent heat loss by reducing the amount of mid-infrared radiation from the body to the environment [61].

Figure 7(o) shows a schematic diagram of the infrared radiation from the human body being reflected by the SiC NFAS. As SiC has a high refractive index and good high-temperature stability, it is an excellent infrared-reflective material [62]. Hence, the infrared radiation of the human body can be reflected back to the skin by the SiC NFAS to maintain the warmth in a cold environment. Likewise, SiC NFAS can effectively reflect external infrared radiation to ensure the safety of human life in a hot environment. In brief, SiC NFAS as an infrared opacifier can effectively reduce infrared radiation and its impact on the human body. The thermal insulation performance of aerogels is affected by solid-phase heat conduction and gas-phase heat convection. The 3D network structure of the SiC NFAS is composed of SiC fibers, and the heat flux along the fibers is hindered when it passes through the limited

contact surface among the SiC fibers, thereby effectively reducing the solid-phase heat conduction. Furthermore, as previously mentioned, there are defects inside the SiC fibers (Fig. S1 in the ESM), which increase the anharmonic vibration of the crystal lattice, resulting in an increased scattering effect on the lattice wave [63]. This decreases the mean free path of phonons and further reduces the solid-phase heat conduction. Moreover, the SiC NFAS has a mesoporous structure, and its pore size is smaller than the mean free path of the air molecules (70 nm). The air molecules in the mesopores of the SiC NFAS are shackled, leading to a reduced gas-phase thermal convection effect. It is noteworthy that the complex physical structure of the SiC NFAS has an obvious scattering effect on infrared rays, which further reduces the heat transfer. Thus, the thermal energy balance of the human body can be effectively regulated by controlling the solid-phase heat conduction, gas-phase heat convection, and heat radiation in the SiC NFAS.

4 Conclusions

A new strategy should be implemented in the field of personal thermal energy regulation equipment to solve the brittleness of polymer-based textiles at low temperatures and the high thermal conductivity of metal fiber textiles woven at high temperatures. Therefore, a multifunctional 3D SiC NFAS for personal thermal management was successfully fabricated via a simple thermal treatment process. The as-prepared SiC NFAS exhibited excellent mechanical properties at low (~−196 ℃) and high temperatures (~700 ℃) with permanent deformation of only 1.3% at room temperature (~20 ℃) after 1000 cycles. The SiC NFAS also exhibited an ultralow thermal conductivity (0.029 W/(m·K)) at room temperature, excellent thermal stability (initial oxidation temperature T_d > 925 ℃), and ultralow density (9 mg/cm^3). Owing to an effective reflection of mid-infrared radiation (2.5–25 μm) by the SiC fibers, the SiC NFAS showed impressive thermal insulation performance. Therefore, the SiC NFAS may be used to adjust the balance of heat energy in the human body because the infrared radiation wavelength (7–14 μm) of the human body is within the mid-infrared wavelength range. This work provides a foundation for the practical application of the SiC NFAS in personal thermal energy regulation. Moreover, the successful preparation of such high-performance material may provide new ideas and insights for the fabrication of multifunctional ceramic aerogels, which could be useful in many futuristic applications.

Acknowledgements

This work was financially supported by the National Natural Science Foundation of China (Nos. U2004177 and U21A2064) and Outstanding Youth Fund of the National Science Fundation of Henan Province (No. 212300410081).

Electronic Supplementary Material

Supplementary material is available in the online version of this article at https://doi.org/10.1007/s40145-022-0606-2.

References

[1] Zhao DL, Lu X, Fan TZ, *et al*. Personal thermal management using portable thermoelectrics for potential building energy saving. *Appl Energ* 2018, **218**: 282–291.
[2] Veselý M, Zeiler W. Personalized conditioning and its impact on thermal comfort and energy performance—A review. *Renew Sust Energ Rev* 2014, **34**: 401–408.
[3] Luo MH, Cao B, Ji WJ, *et al*. The underlying linkage between personal control and thermal comfort: Psychological or physical effects? *Energ Buildings* 2016, **111**: 56–63.
[4] Axelrod YK, Diringer MN. Temperature management in acute neurologic disorders. *Neurol Clin* 2008, **26**: 585–603.
[5] Brown DJA, Brugger H, Boyd J, *et al*. Accidental hypothermia. *N Engl J Med* 2012, **367**: 1930–1938.
[6] Chan APC, Yi W. Heat stress and its impacts on occupational health and performance. *Indoor Built Environ* 2016, **25**: 3–5.
[7] Peng YC, Cui Y. Advanced textiles for personal thermal management and energy. *Joule* 2020, **4**: 724–742.
[8] Hsu PC, Liu XG, Liu C, *et al*. Personal thermal management by metallic nanowire-coated textile. *Nano Lett* 2015, **15**: 365–371.
[9] Xie Z, Jin XJ, Chen G, *et al*. Integrated smart electrochromic windows for energy saving and storage applications. *Chem Commun* 2014, **50**: 608–610.
[10] Tong JK, Huang XP, Boriskina SV, *et al*. Infrared-transparent visible–opaque fabrics for wearable personal thermal management. *ACS Photonics* 2015, **2**: 769–778.
[11] Guo YB, Li KR, Hou CY, *et al*. Fluoroalkylsilane-modified textile-based personal energy management device for multifunctional wearable applications. *ACS Appl Mater Interfaces* 2016, **8**: 4676–4683.
[12] Yang L, Yan HY, Lam JC. Thermal comfort and building

energy consumption implications—A review. *Appl Energ* 2014, **115**: 164–173.

[13] Kou JL, Jurado Z, Chen Z, *et al*. Daytime radiative cooling using near-black infrared emitters. *ACS Photonics* 2017, **4**: 626–630.

[14] Zhang H, Arens E, Zhai YC. A review of the corrective power of personal comfort systems in non-neutral ambient environments. *Build Environ* 2015, **91**: 15–41.

[15] Zhai Y, Ma YG, David SN, *et al*. Scalable-manufactured randomized glass–polymer hybrid metamaterial for daytime radiative cooling. *Science* 2017, **355**: 1062–1066.

[16] De Korte EM, Spiekman M, Hoes-van Oeffelen L, *et al*. Personal environmental control: Effects of pre-set conditions for heating and lighting on personal settings, task performance and comfort experience. *Build Environ* 2015, **86**: 166–176.

[17] Hoyt T, Arens E, Zhang H. Extending air temperature setpoints: Simulated energy savings and design considerations for new and retrofit buildings. *Build Environ* 2015, **88**: 89–96.

[18] Freire RZ, Oliveira GHC, Mendes N. Predictive controllers for thermal comfort optimization and energy savings. *Energ Buildings* 2008, **40**: 1353–1365.

[19] Choi S, Park J, Hyun W, *et al*. Stretchable heater using ligand-exchanged silver nanowire nanocomposite for wearable articular thermotherapy. *ACS Nano* 2015, **9**: 6626–6633.

[20] Claramunt S, Monereo O, Boix M, *et al*. Flexible gas sensor array with an embedded heater based on metal decorated carbon nanofibres. *Sens Actuat B Chem* 2013, **187**: 401–406.

[21] Amjadi M, Kyung KU, Park I, *et al*. Stretchable, skin-mountable, and wearable strain sensors and their potential applications: A review. *Adv Funct Mater* 2016, **26**: 1678–1698.

[22] Hong S, Gu Y, Seo JK, *et al*. Wearable thermoelectrics for personalized thermoregulation. *Sci Adv* 2019, **5**: eaaw0536.

[23] Cai LL, Peng YC, Xu JW, *et al*. Temperature regulation in colored infrared-transparent polyethylene textiles. *Joule* 2019, **3**: 1478–1486.

[24] Tian RM, Liu YQ, Koumoto K, *et al*. Body heat powers future electronic skins. *Joule* 2019, **3**: 1399–1403.

[25] Roh JS, Chi YS, Kang TJ. Thermal insulation properties of multifunctional metal composite fabrics. *Smart Mater Struct* 2009, **18**: 025018.

[26] Yue XJ, Zhang T, Yang DY, *et al*. Ag nanoparticles coated cellulose membrane with high infrared reflection, breathability and antibacterial property for human thermal insulation. *J Colloid Interface Sci* 2019, **535**: 363–370.

[27] Hsu PC, Song AY, Catrysse PB, *et al*. Radiative human body cooling by nanoporous polyethylene textile. *Science* 2016, **353**: 1019–1023.

[28] Peng YC, Chen J, Song AY, *et al*. Nanoporous polyethylene microfibres for large-scale radiative cooling fabric. *Nat Sustain* 2018, **1**: 105–112.

[29] Cai LL, Song AY, Li W, *et al*. Spectrally selective nanocomposite textile for outdoor personal cooling. *Adv Mater* 2018, **30**: 1802152.

[30] Caps R, Arduini-Schuster MC, Ebert HP, *et al*. Improved thermal radiation extinction in metal coated polypropylen microfibers. *Int J Heat Mass Transf* 1993, **36**: 2789–2794.

[31] Dombrovsky LA. Infrared and microwave radiative properties of metal coated microfibres. *Revue Générale de Thermique* 1998, **37**: 925–933.

[32] Kleiman M, Gurwich I, Shiloah N. Enhanced extinction of electromagnetic radiation by metal-coated fibers. *J Quant Spectrosc Radiat Transf* 2007, **106**: 184–191.

[33] Zhao Y, Hao LL, Zhang XD, *et al*. A novel strategy in electromagnetic wave absorbing and shielding materials design: Multi-responsive field effect. *Small Sci* 2022, **2**: 2100077.

[34] Wang F, Gu WH, Chen JB, *et al*. The point defect and electronic structure of K doped $LaCo_{0.9}Fe_{0.1}O_3$ perovskite with enhanced microwave absorbing ability. *Nano Res* 2022, **15**: 3720–3728.

[35] Wang GH, Zhao Y, Yang F, *et al*. Multifunctional integrated transparent film for efficient electromagnetic protection. *Nano-Micro Lett* 2022, **14**: 65.

[36] Peng Y, Guo ZN, Yang JJ, *et al*. Enhanced photocatalytic H_2 evolution over micro-SiC by coupling with CdS under visible light irradiation. *J Mater Chem A* 2014, **2**: 6296–6300.

[37] Lu D, Su L, Wang HJ, *et al*. Scalable fabrication of resilient SiC nanowires aerogels with exceptional high-temperature stability. *ACS Appl Mater Interfaces* 2019, **11**: 45338–45344.

[38] Wu RB, Zhou K, Yang ZH, *et al*. Molten-salt-mediated synthesis of SiC nanowires for microwave absorption applications. *CrystEngComm* 2013, **15**: 570–576.

[39] Peng K, Zhou JX, Gao HF, *et al*. Emerging one-/two-dimensional heteronanostructure integrating SiC nanowires with MoS_2 nanosheets for efficient electrocatalytic hydrogen evolution. *ACS Appl Mater Interfaces* 2020, **12**: 19519–19529.

[40] Dai W, Yu JH, Wang Y, *et al*. Enhanced thermal conductivity for polyimide composites with a three-dimensional silicon carbide nanowires@graphene sheets filler. *J Mater Chem A* 2015, **3**: 4884–4891.

[41] Lin LW. Synthesis and optical property of large-scale centimetres-long silicon carbide nanowires by catalyst-free CVD route under superatmospheric pressure conditions. *Nanoscale* 2011, **3**: 1582–1591.

[42] Du B, Zhang DY, Qian JJ, *et al*. Multifunctional carbon nanofiber-SiC nanowire aerogel films with superior microwave absorbing performance. *Adv Compos Hybrid Mater* 2021, **4**: 1281–1291.

[43] Cheng YH, Hu P, Zhou SB, *et al*. Achieving tunability of effective electromagnetic wave absorption between the whole X-band and Ku-band via adjusting PPy loading in SiC nanowires/graphene hybrid foam. *Carbon* 2018, **132**: 430–443.

[44] Liang HW, Guan QF, Chen LF, *et al*. Macroscopic-scale template synthesis of robust carbonaceous nanofiber hydrogels and aerogels and their applications. *Angew Chem Int Ed* 2012, **51**: 5101–5105.

[45] Ye XL, Chen ZF, Zhang JX, *et al*. SiC network reinforced SiO_2 aerogel with improved compressive strength and preeminent microwave absorption at elevated temperatures. *Ceram Int* 2021, **47**: 31497–31505.

[46] Su L, Wang HJ, Niu M, *et al*. Ultralight, recoverable, and high-temperature-resistant SiC nanowire aerogel. *ACS Nano* 2018, **12**: 3103–3111.

[47] Si Y, Yu JY, Tang XM, *et al*. Ultralight nanofibre-assembled cellular aerogels with superelasticity and multifunctionality. *Nat Commun* 2014, **5**: 5802.

[48] Su L, Wang HJ, Niu M, *et al*. Anisotropic and hierarchical SiC@SiO_2 nanowire aerogel with exceptional stiffness and stability for thermal superinsulation. *Sci Adv* 2020, **6**: eaay6689.

[49] Cheng XD, Zhu SY, Pan YL, *et al*. Fire retardancy and thermal behaviors of cellulose nanofiber/zinc borate aerogel. *Cellulose* 2020, **27**: 7463–7474.

[50] Guerrero-Alburquerque N, Zhao SY, Adilien N, *et al*. Strong, machinable, and insulating chitosan–urea aerogels: Toward ambient pressure drying of biopolymer aerogel monoliths. *ACS Appl Mater Interfaces* 2020, **12**: 22037–22049.

[51] Zhou T, Cheng XD, Pan YL, *et al*. Mechanical performance and thermal stability of polyvinyl alcohol–cellulose aerogels by freeze drying. *Cellulose* 2019, **26**: 1747–1755.

[52] Cheng YH, Zhou SB, Hu P, *et al*. Enhanced mechanical, thermal, and electric properties of graphene aerogels via supercritical ethanol drying and high-temperature thermal reduction. *Sci Rep* 2017, **7**: 1439.

[53] Guzel Kaya G, Yilmaz E, Deveci H. Synthesis of sustainable silica xerogels/aerogels using inexpensive steel slag and bean pod ash: A comparison study. *Adv Powder Technol* 2020, **31**: 926–936.

[54] Shi MK, Shen MM, Guo XY, *et al*. $Ti_3C_2T_x$ MXene-decorated nanoporous polyethylene textile for passive and active personal precision heating. *ACS Nano* 2021, **15**: 11396–11405.

[55] Morkoç H, Strite S, Gao GB, *et al*. Large-band-gap SiC, III–V nitride, and II–VI ZnSe-based semiconductor device technologies. *J Appl Phys* 1994, **76**: 1363–1398.

[56] Wu Y, Zhou LP, Du XZ, *et al*. Optical and thermal radiative properties of plasmonic nanofluids containing core–shell composite nanoparticles for efficient photothermal conversion. *Int J Heat Mass Transf* 2015, **82**: 545–554.

[57] Hillenbrand R, Taubner T, Keilmann F. Phonon-enhanced light–matter interaction at the nanometre scale. *Nature* 2002, **418**: 159–162.

[58] Riedl C, Coletti C, Starke U. Structural and electronic properties of epitaxial graphene on SiC(0001): A review of growth, characterization, transfer doping and hydrogen intercalation. *J Phys D Appl Phys* 2010, **43**: 374009.

[59] Hardy JD, Dubois EF. Regulation of heat loss from the human body. *PNAS* 1937, **23**: 624–631.

[60] Winslow CEA, Gagge AP, Herrington LP. The influence of air movement upon heat losses from the clothed human body. *Am J Physiol Leg Content* 1939, **127**: 505–518.

[61] Hazarika A, Deka BK, Kim DY, *et al*. Woven kevlar fiber/polydimethylsiloxane/reduced graphene oxide composite-based personal thermal management with freestanding Cu–Ni core–shell nanowires. *Nano Lett* 2018, **18**: 6731–6739.

[62] Younes J, Harajli Z, Soueidan M, *et al*. Mid-IR photothermal beam deflection technique for fast measurement of thermal diffusivity and highly sensitive subsurface imaging. *J Appl Phys* 2020, **127**: 173101.

[63] Yan F, Devaty RP, Choyke WJ, *et al*. Anharmonic vibrations of the dicarbon antisite defect in 4H-SiC. *Appl Phys Lett* 2012, **100**: 132107.